# Imaging Topological Spin Structures Using Light-Polarization and Magnetic Microscopy

Till Lenz, Georgios Chatzidrosos, Zhiyuan Wang, Lykourgos Bougas, Yannick Dumeige, Arne Wickenbrock, Nico Kerber, Jakub Zázvorka, Fabian Kammerbauer, Mathias Kläui, Zeeshawn Kazi, Kai-Mei C. Fu, S, 6, Kohei M. Itoh, Hideyuki Watanabe, and Dmitry Budker, Helmholtz Institut Mainz, Johannes Gutenberg-Universität Mainz, Mainz 55128, Germany

Institut für Physik, Johannes Gutenberg-Universität Mainz, Mainz 55128, Germany

Université de Rennes, CNRS, Institut FOTON UMR 6082, Lannion F-22305, France

Institute of Physics, Faculty of Mathematics and Physics, Charles University, Prague 121 16, Czech Republic

Physics Department, University of Washington, Seattle, Washington 98105, USA

<sup>6</sup> Electrical and Computer Engineering Department, University of Washington, Seattle, Washington 98105, USA

<sup>7</sup> Helmholtz Institut Mainz, Johannes Gutenberg University, Mainz 55128, Germany

<sup>8</sup> Spintronics Research Center, Keio University, 3-14-1 Hiyoshi, Kohoku-ku, Yokohama 223-8522, Japan

<sup>9</sup> Device Technology Research Institute, National Institute of Advanced Industrial Science and Technology, Tsukuba Central 2, 1-1-1 Umezono, Tsukuba, Ibaraki 305-8568, Japan

Department of Physics, University of California, Berkeley, California 94720-300, USA



(Received 11 November 2020; revised 30 December 2020; accepted 13 January 2021; published 17 February 2021)

We present an imaging modality that enables detection of magnetic moments and their resulting stray magnetic fields. We use wide-field magnetic imaging that employs a diamond-based magnetometer and has combined magneto-optic detection (e.g., magneto-optic Kerr effect) capabilities. We employ such an instrument to image magnetic (stripe) domains in multilayered ferromagnetic structures.

DOI: 10.1103/PhysRevApplied.15.024040

# I. INTRODUCTION

An understanding of the behavior of spins and charges in magnetic systems is at the heart of condensed-matter physics. As a consequence intense ongoing research activities are focused on developing and understanding their behavior. This understanding is key toward the generation of faster, smaller, and more energy-efficient magnetic technologies [1,2].

The success of all research activities relies on advances in theory and materials synthesis but most critically on sensitive probes. These allow for the determination of their static and dynamic spin configurations and current distributions, which enable an improved understanding of the interplay between the spin-spin and spin-orbit interactions in these systems. To achieve this, several powerful techniques for real-space probing of magnetic structures are employed, such as spin-polarized low-energy electron microscopy [3,4] and x-ray magnetic circular dichroism [5,6], both of which are sensitive to the magnetization distribution of the structures.

An alternative approach is the detection of the stray magnetic fields generated by the magnetic textures. Techniques such as magnetic-resonance-force microscopy [7,8] and scanning magnetometry using superconducting quantum interference devices (SQUIDs) [9,10], allow for real-space imaging of the stray magnetic fields emanating from magnetic structures. However, these techniques typically operate over a narrow range of environmental conditions and in some cases can have magnetic (perturbative) back action on the devices under investigation.

Magnetometry based on the electron spin of nitrogen-vacancy (N-V) defects in diamond has emerged as a versatile, highly sensitive stray-field probe for the noninvasive study of magnetic systems [11]. Diamond-based magnetometers can operate from cryogenic to above-room-temperature environments, have a dynamic range spanning at least nine decades (dc to gigahertz), and allow for sensor-sample distances as small as a few nanometers. With this, they provide access to static and dynamic magnetic and/or electric phenomena with diffraction-limited to nanoscale spatial resolution depending on the imaging modality. Most crucially, N-V-based magnetometry is magnetically nonperturbative and works under a wide range of external magnetic and electric fields.

<sup>\*</sup>lybougas@uni-mainz.de

<sup>†</sup>budker@uni-mainz.de

Scanning N-V-based magnetic microscopy utilizes a diamond nanocrystal that hosts a single N-V center attached to the tip of an atomic force microscope and has already been successfully applied in studies of emerging magnetic phenomena. Prominent examples are the case of nanoscale imaging and control of domain-wall hopping in ultrathin ferromagnets [12] and magnetic wires [13], imaging of the noncollinear antiferromagnetic order in magnetic thin films [14], the direct measurement of the interfacial Dzyaloshinskii-Moriya interaction in ferromagnetic multilayer heterostructures [15], and even in identifying the morphology of isolated skyrmions in ultrathin magnetic films [16,17]. Scanning N-V-based magnetometry is highly sensitive and produces magnetic field maps of a sample with spatial resolution ultimately limited by the atomic size of the tip. However, similarly to magnetic force microscopy, its operation requires specific environmental conditions and is not suitable for wide-field inspection of dynamics at fast time scales (of the order of milliseconds). An alternative is wide-field N-V-based magnetic microscopy, which employs ensembles of N-V centers within a diamond crystal and allows for magnetic imaging with an unprecedented combination of temporal (millisecond) and spatial (diffraction-limited) resolution. State-of-the-art experimental demonstrations have demonstrated sub- $\mu T \mu m / \sqrt{Hz}$  magnetometric sensitivities over wide fields of view (FOVs) (as large as approximately 1 mm<sup>2</sup>) [18–21].

An additional merit in using N-V-based magnetometry is the possibility of simultaneously measuring all Cartesian components of static and/or dynamic magnetic fields [18,22]. This becomes vital when one wishes to identify, for instance, the type and the chirality of domain walls of skyrmions in magnetic multilayer stacks [12,23]. However, even with the employment of vector magnetometric protocols, reconstruction of the magnetic spinstructure topology based on the detected stray magnetic fields is an underconstrained inverse problem [11,23,24]. In other words, this means that an infinite number of magnetic topologies can give rise to similar stray magnetic field patterns. Therefore, a straightforward solution is the implementation of a detection modality that enables the detection of both the magnetization and its resulting stray magnetic fields.

We present here an imaging modality that allows for the detection of both magnetic moments and their resulting stray magnetic fields. Such an imaging system consists of a polarization-sensitive epifluorescent microscope that incorporates a diamond sensor and exploits the radiation required for the magnetometric measurements to perform magneto-optic Kerr effect (MOKE) measurements [25]. Such an instrument allows for combined detection of magnetization and its resultant stray magnetic fields, while being magnetically nonperturbative and operable over a broad temperature range, making it an ideal tool for the

study of magnetic structures and their dynamics under a wide range of environmental conditions. We wish to emphasize here that a MOKE measurement is an indirect way of detecting the magnetic moments via changes in the polarization of light upon reflection of a magnetic surface. However, this polarization signal can be translated to magnetization using the specific Kerr constant of the material, which we can obtain, for instance, using a SQUID-based calibration measurement.

# II. PRINCIPLES OF MAGNETO-OPTICAL AND WIDE-FIELD MAGNETIC IMAGING

# A. N-V-based magnetic imaging

The N-V center in diamond consists of a substitutional nitrogen atom in the carbon lattice adjacent to a vacancy. The negatively charged N-V center (N-V<sup>-</sup>) has an electronic spin-triplet ground state ( ${}^{3}A_{2}$ ; S=1) with magnetic Zeeman sublevels  $m_s = \{-1, 0, +1\}$  (quantized along the N-V binding axis). Moreover, it has an axial zero-field splitting of approximately 2.87 GHz between the  $m_s = 0$ and  $m_s = \pm 1$  sublevels, the energies of which shift in response to local magnetic fields, crystal stress, temperature changes, and electric fields [Fig. 1(a)]. The spin state of the N-V center can be initialized (polarized to the  $m_s = 0$ sublevel) using (continuous or pulsed) optical excitation (typically with  $\lambda = 532$  nm) and readout through spindependent photoluminescence (PL): the  $m_s = 0$  sublevel exhibits a higher fluorescence rate under illumination than the  $m_s = \pm 1$  sublevels. The application of a small external magnetic field along the N-V quantization axis lifts the degeneracy of the  $m_s = \pm 1$  magnetic sublevels and magnetic field measurements are consequently possible via the precise measurement of the N-V spin-resonance frequencies. This is typically done by sweeping the frequency of an externally applied microwave (MW) driving field while monitoring the spin-dependent photoluminescence, thus allowing for N-V-fluorescence-based magnetometry by optically detected magnetic resonance (ODMR) spectroscopy. Alternative magnetometric modalities that rely on absorption- or photocurrent-based detection schemes [26,27] also exist but are not employed in this work. In high-quality diamond sensors, the attainable ODMR line width is narrow enough to observe the hyperfine structure of the N-V center, i.e., the coupling between the host nitrogen nucleus (99.6% of <sup>14</sup>N in natural abundance, for which  $I_N = 1$ ) and the unpaired N-V electron spin. For the case of <sup>14</sup>N, every observed ODMR peak splits into a triplet with a separation of  $A_{\rm hfs} \approx 2.16$  MHz [28] [Fig. 1(a)].

Using ensembles of N-V centers, it is possible to perform highly sensitive magnetic imaging using wide-field (e.g., epifluorescence) optical microscopy. In such a case, a thin layer of N-V centers is typically engineered close to the surface of a diamond crystal. This layer is then used for two-dimensional mapping of the

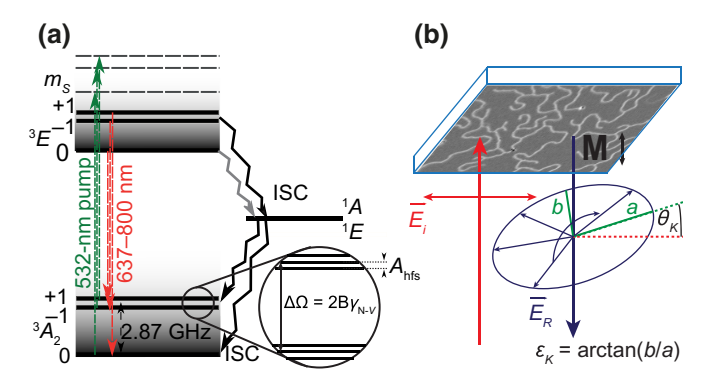


FIG. 1. (a) The N-V energy-level diagram. (b) A schematic of the polar MOKE.  $\vec{E}_i$  describes the linearly polarized incident light and  $\vec{E}_R$  the reflected light with rotation angle  $\Theta_K$  and ellipticity  $\varepsilon_K$ .

magnetic field generated by a sample proximal to the surface of the diamond, by projecting the N-V fluorescence onto a camera sensor and performing ODMR measurements [29]. As such, submicrometer-resolved magnetic field maps can be achieved using high magnification and high-numerical-aperture (NA) microscopes equipped with, for example, a common charged-coupled device (CCD) or complementary-metal-oxide-semiconductor (CMOS) camera. Furthermore, N-V centers are oriented along one of four crystallographic (111) directions within the diamond crystal lattice (in particular, along the (111), (111),  $\langle 11\overline{1}\rangle$ , and  $\langle \overline{1}11\rangle$  crystal axes; see the inset to Fig. 2). A diamond crystal hosting an ensemble of N-V centers typically contains an equal number of N-V centers for each direction. As such, ODMR spectra from all N-V orientations yield the necessary information to reconstruct vector magnetic field components from magnetized structures proximal to the N-V centers. Wide-field N-V-based imaging techniques have already been used to image magnetic fields generated by magnetic thin films [30], nanoparticles [31], and vortices in type-II superconductors [32], and even to reconstruct the current flow inside integrated circuits [33] or graphene field-effect transistors [34].

# B. Magneto-optical imaging

Magneto-optical effects from magnetized media can be observed via transmission- or reflection-based measurements. The optical effects that manifest themselves when light is reflected from the surface of a magnetized material are conventionally designated as MOKEs. MOKE microscopy, i.e., a technique capable of studying MOKE with the use of an optical microscope, is one of the most prominent tools for the spatiotemporal visualization of distributions of magnetization (M) within magnetic materials [25]. In general, Kerr effects manifest as changes of the intensity and/or the plane of polarization ( $\Theta_K$ ) and the ellipticity ( $\varepsilon_K$ ) of incident linearly polarized light upon

reflection. All the different types of Kerr effects (polar, longitudinal, and transverse) mostly scale linearly with magnetization (higher-order quadratic effects can also be observed using MOKE microscopy [25]; in this work we will focus on samples that show no quadratic MOKE and for this reason we will assume MOKE to be linear in the magnetization of a sample). As such, investigation of the magnetization of a magnetic sample becomes possible with the use of a simple optical microscope that consists of a polarization-selection and a polarization-analysis step. For most cases of interest, as in our work here, the polar type of MOKE is typically studied, which means that one senses the magnetization component perpendicular to the surface of the sample [Fig. 1(b)]. Moreover, the polar MOKE manifests as a change both in polarization angle  $(\Theta_K)$ and ellipticity  $(\varepsilon_K)$ , while the reflected intensity remains unchanged.

# C. Combined MOKE and magnetic-imaging microscopy

The combination of both imaging modalities, N-V-based magnetic and MOKE, is made possible by the additional incorporation of polarization-sensitive preparation and analysis steps in the optical setup required to perform N-V-based magnetic imaging. In particular, by preselecting the polarization state of the optical excitation required for the N-V-based magnetometric protocol (i.e., green laser light) and imaging changes in its polarization state upon reflection from a magnetized sample placed upon the diamond crystal, while simultaneously imaging the N-V fluorescence, one obtains a combined image of magnetization and their resulting magnetic fields.

# III. EXPERIMENTAL METHODS

# A. Magnetic sample

To demonstrate the capabilities of an imaging setup that can perform measurements of magnetization and magnetic fields, we use a multilayered ferromagnetic structure that shows rich topological magnetic structures (magnetic domains) under the influence of external magnetic fields.

The sample is a  $Ta(5 \text{ nm})/Co_{20}Fe_{60}B_{20}(1 \text{ nm})/Ta(0.08 \text{ nm})/MgO(2 \text{ nm})/Ta(5 \text{ nm})$  material stack that is grown on a Si/SiO<sub>2</sub> substrate (500- $\mu$ m thickness) by demagnetron sputtering. The use of a Singulus Rotaris sputtering system allows us to tune the thickness of the layers with high accuracy (reproducibility better than 0.01 nm) [35]. The Ta(0.08 nm) insertion layer, which is not even a complete Ta monolayer, is inserted to fine tune the perpendicular (out-of-plane) magnetic anisotropy (see the inset Fig. 2, left-hand side) stemming from the  $Co_{20}Fe_{60}B_{20}$ -MgO interface [36]. This allows us to get closer to the spin-reorientation transition [37]. Thereby, we can achieve a typical hourglass-shaped hysteresis loop indicating the

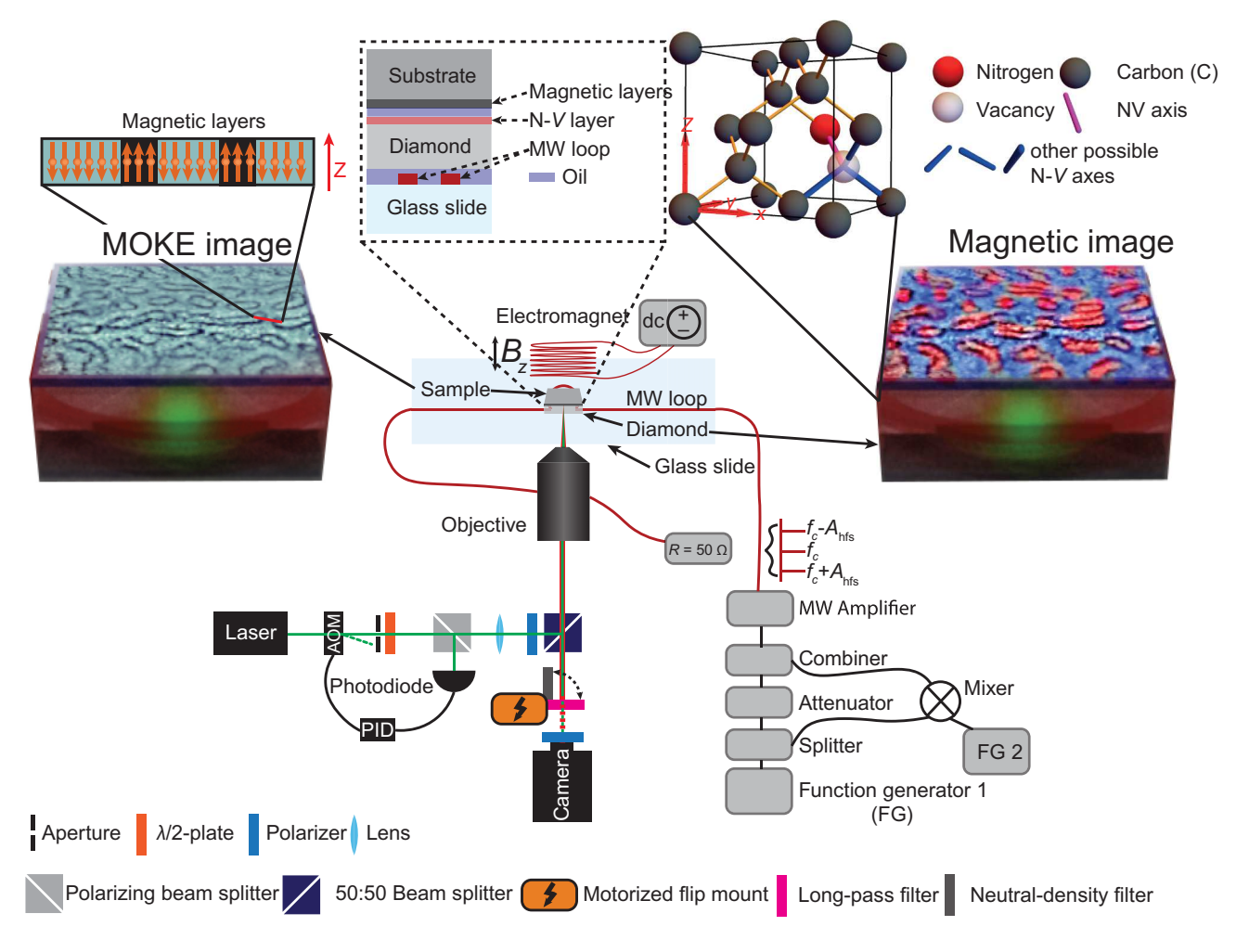


FIG. 2. A schematic of the experimental setup. Top left: an example of a MOKE image, with the inset depicting a magnetic sample having an out-of-plane anisotropy. Center: the experimental arrangement of the diamond sensor and the magnetic sample (resting upon a microscope slide); the inset shows a detailed view of the different layers indicating the arrangement of diamond sensor and the magnetic sample. Top right: an inset showing a unit cell of the diamond lattice containing a single N-V center and indicating all other possible N-V orientations. Bottom left: the optical setup for combined MOKE and N-V-based imaging. Bottom right: the MW setup used to drive transitions among the ground-state spin sublevels of the N-V center.

presence of magnetic domains or a skyrmion phase [38]. Using SQUID-based measurements, we determine the saturation magnetization of the sample to be  $M_s \approx 760 \text{ kA/m}$ at room temperature.

# **B.** Experimental setup 1. Optical setup

In Fig. 2, we present the experimental setup that we use for combined magnetic field (N-V) and magnetization (MOKE) measurements. The basis of the setup is a home-built inverted-epifluorescence microscope.

As light source for both the magnetometric protocol and the light-polarization measurements, we use a 532-nm diode laser (Laser Quantum, Gem 532 nm). The laser intensity is stabilized with a feedback system using an acousto-optical modulator (AOM, ISOMET-1260C, with an ISOMET 630C-350 driver) controlled with a proportional-integral-derivative (PID) controller (SRS SIM960). The excitation and reflected and PL beams are split using a 50:50 beam-splitter cube (BSC) before the objective. To operate in wide-field configuration, another lens (f = 150 mm) is placed before BSC, which leads to an enlarged excitation area.

The imaging system consists of an air objective (Olympus UplanFL N 60X) with a magnification of 60x, a working distance of 0.2 mm, and a correction collar that allows us to compensate for cover-glass thicknesses of 0.11-0.23 mm. As detector, we use a scientific CMOS (sCMOS) camera (Andor Zyla 5.5) with a pixel area of  $6.5 \times 6.5 \,\mu\text{m}^2$ . This leads to an effective pixel area of approximately  $108 \times 108$  nm<sup>2</sup> in the focal plane, i.e., on the sample. The home-built sample holder consists of a thickness 0 (approximately  $85 - 115 \mu m$ ) coverslip, which is glued onto a printed circuit board that is supported upon a three-dimensional translation stage. The coverslip is electroplated with a copper layer, from which an  $\Omega$ -shaped strip line is produced. This strip line is used to deliver the MW fields required for N-V-based magnetometry. The FOV is adjusted in such a way that it resides in the center of the omega loop. On top of the coverslip, we place our diamond sensor and, on top of the diamond sensor, the magnetic sample under investigation. The diamond sample is oriented in such a way that the N-V layer is proximal to the magnetic layers of the sample (see the inset to Fig. 2). To fix the samplesensor distance to values less than 10  $\mu$ m, and to reduce lateral movement and the amount of aberrations, we use microscope immersion oil between the coverslip-diamond and diamond-sample surfaces. A detailed schematic of the diamond-sensor and magnetic sample configuration is shown as an inset in Fig. 2. The laser beam enters and exits the diamond through the coverslip.

To image the N-V PL, we use a 650-nm long-pass filter (FEL0650, Thorlabs) to remove the reflected green light. For MOKE imaging, we remove the long-pass filter and introduce a neutral-density filter (optical density = 3) before the camera. This is done to coarsely match the amount of reflected photons from the green laser beam to the number of detected photons in the observed N-V fluorescence (under typical experimental conditions). This facilitates operation (i.e., the use of similar acquisition settings), while sacrificing optimal polarimetric sensitivities.

# 2. Magnetic sensor

For wide-field N-V magnetic imaging, we use a near-surface high-density N-V ensemble. In particular, a 100 nm<sup>14</sup>N doped, isotope-purified (99.9% <sup>12</sup>C) layer is grown by chemical-vapor deposition on an electronic grade diamond substrate (Element Six). The sample is then implanted with 25 keV He<sup>+</sup> at a dose of  $10^{12}$  ions/cm<sup>2</sup> to form vacancies, followed by a vacuum anneal at  $900\,^{\circ}$ C for 2 h for N-V formation and an anneal in O<sub>2</sub> at 425  $^{\circ}$ C for 2 h for charge-state stabilization [39]. The resulting ensemble has an N-V density of approximately  $1.2 \times 10^{17}$  cm<sup>-3</sup>. This value is obtained by comparing the fluorescence of the layer to the average of near-surface single N-V centers in a control sample. The diamond crystal has dimensions of  $2 \times 2$  mm<sup>2</sup> and a thickness of approximately  $90 - 100~\mu$ m.

# 3. External fields

To generate the magnetic domains in the sample, we apply a bias magnetic field  $(B_z)$  with the use of a coil (length 2.8 cm, radius 3 cm, producing approximately 6 G/A). The coil is supplied with dc current using a computer-controlled power supply.

To perform the N-V-based magnetic imaging, a MW source and/or function generator (SRS SG384) is used. The MW signal is split and mixed with a 2.16-MHz signal and then combined again, in order to resonantly address and drive all (three) hyperfine-resolved N-V spin resonances simultaneously. This allows us to obtain full-contrast ODMR spectra without the drawback of power broadening and, thus, yields improved magnetometric sensitivities [40]. All MW frequency components are amplified with a 16-W (+43-dB) amplifier (ZHL-16W-43+) and passed through a circulator (Pasternack CS-3.000) and a high-pass filter (Mini Circuits VHP-9R5) before they are transmitted through the omega-shaped strip line. A schematic of the setup required to generate the external fields is presented in Fig. 2.

# 4. Polarization control

To perform MOKE imaging in polar configuration, the setup is equipped with two linear polarizers (Thorlabs LPVISA100): one is placed in front of the BSC to prepare the green light with linear polarization (it also enables optimization of the magnetometric protocol through the appropriate selection of polarization). The second one, hereafter called the analyzer, is used for analysis of the polarization state of the reflected light beam and is placed directly in front of the camera. The rotation angle of the analyzer with respect to the polarizer is optimized to obtain the best signal-to-noise ratio (SNR) for MOKE measurements. For the present experimental conditions, this optimum is found when the analyzer is nearly crossed with the polarizer.

To allow for switching between magnetic field and magnetization imaging, a computer-controlled flip mount is positioned in front of the analyzer, which allows us to switch from using the long-pass filter (and thus performing magnetic field measurements) to using the neutral-density filter (allowing for MOKE measurements).

# C. Magnetic imaging

In order to obtain quantitative images of the local magnetic field, it is necessary to acquire ODMR spectra for all pixels within the illuminated FOV. Here, we employ a continuous-wave (cw) technique for N-V ODMR-based magnetic imaging, wherein optical N-V spin polarization, MW drive, and spin-state readout via the N-V PL occur simultaneously. The diamond sensor is continuously illuminated with approximately 80 mW of 532 nm laser light and the resulting N-V PL is collected using the objective of the microscope.

For each frequency point of the N-V ODMR spectrum  $(\nu_i)$ , PL images are captured and normalized by images captured at a fixed off-resonant frequency (in our case,  $\nu_{\rm off} = 2.16$  GHz). The number of detected photons on each pixel at  $\nu_i$  is then divided by the detected photon number at  $\nu_{\rm off}$  for the same pixel. This sequence is then repeated

between 15 and 40 times (for every selected  $v_i$ ); a typical exposure time is 100 ms per sequence.

Here, we aim to image fields from a sample with a perpendicular (out-of-plane) magnetic anisotropy. The bias magnetic field required to manipulate samples with this anisotropy is applied along the (100) axis of the diamond crystal. As such, the applied field and the resulting magnetic fields from the magnetic structure lead to (almost) equal magnetic field projections along all (eight) different N-V orientations (along four axes) in our diamond sample. This can easily be shown by calculating the scalar product between the different possible N-V axes ( $\langle 111 \rangle$ ,  $\langle 111 \rangle$ ,  $\langle 111 \rangle$ , and  $\langle 111 \rangle$ ) and the  $\langle 100 \rangle$  direction describing the magnetic field. This, in turn, results in degenerate magnetic eigenstates and, thus, equal transition frequencies in addressing N-V centers along the different axes. In fact, the magnetic stray fields generated by the sample are not exactly oriented along the applied field but since the splitting created by transverse components is smaller than the line width, this results only in broadening of the resonances. As mentioned earlier, due to hyperfine interactions this results in two sets of three transition frequencies, which are separated by  $2\gamma_{N-V}B_{N-V}$  ( $\gamma_{N-V}\approx$ 28 MHz/mT and  $B_{N-V}$ : projection of the magnetic field along the N-V axis). In order to increase the sensitivity of our sensor, we simultaneously apply three frequency components with a fixed separation of 2.16 MHz, matching the hyperfine splitting of the resonances. This applied frequency triplet is then scanned over the three N-V resonances and, thus, results in five dips for both  $\Delta m_s = \pm 1$ transition families. The relative amplitude ratios between the five observed Lorentzian features in the ODMR spectrum are 1:2:3:2:1 [see Fig. 3(c) and Ref. [40]]. This is a result of the fact that at different carrier frequencies, one, two, or three hyperfine components of the transitions are on resonance with the MW driving fields. For this reason, the observed features in the obtained ODMR spectra are fitted with two sets of five Lorentzians. In the general case of an arbitrarily oriented magnetic field, eight sets of five Lorentzians are observable. Overall, by determining their frequency separation, we can image the local magnetic field perpendicular to the diamond surface. We determine the average magnetometric sensitivity of our current setup to be  $\delta B_{N-V} \approx 2\mu T \mu m / \sqrt{Hz}$ within a FOV of approximately  $40 \times 40 \mu m^2$ , which is mainly limited by mechanical instabilities of the setup.

# D. MOKE imaging

MOKE images of the sample-magnetization topology are taken in a similar fashion to the magnetic images after switching to MOKE operation by using the flip mount. This allows for the collection of the green laser light instead of the N-V PL.

For a given strength of the externally applied magnetic field required to change the magnetization state of the sample, we obtain a MOKE signal for each pixel by averaging over 50 acquisition cycles of the camera (typical exposure time 10 ms per cycle). This average is then normalized to an equivalent measurement performed at a reference field  $|B_{ref}| > |B_{sat}|$  [i.e.,  $S_{MOKE} = [N_{ph}(B_z) N_{\rm ph}(B_{\rm ref})]/N_{\rm ph}(B_{\rm ref})$ ]. In our case,  $B_{\rm sat}$ , the saturation field at which the magnetic sample is in a monodomain state with all the domains and spins aligned with the external magnetic field is approximately  $B_{\rm sat} \approx 1$  mT. This comparison with a reference image allows us to eliminate beam-intensity variations in the FOV, the effect of impurities and/or surface features, and birefringence in the diamond crystal. We determine the polarimetric angleimaging sensitivity of our current setup to be  $\delta\Theta_K \approx$ 50  $\mu$ rad  $\mu$ m/ $\sqrt{Hz}$  (again mainly limited by mechanical instabilities of the setup).

## IV. RESULTS

In Fig. 3, we show the main result of this work. Figure 3(a) shows the hysteresis magnetization curve of our magnetic sample obtained by implementing a MOKE measurement sequence and by averaging over all pixel values within the FOV. For each strength of the externally applied magnetic field ( $B_z$ ), which is used to generate the magnetization curve [for comparison, we also present measurements obtained using a commercial MOKE microscope (Evico GmbH)]. In Fig. 3(b), we show a MOKE image of the sample-magnetization topology under an externally applied magnetic field strength of  $B_z = 0.329$  mT, demonstrating our ability to observe magnetic (stripe) domains and qualitatively image their magnetization.

In Fig. 3(c), we present the magnetic field map generated by the stripe domains as obtained by N-V-based magnetic imaging. Using the differences between the resonance frequencies observed in the recorded ODMR spectra, we obtain the direction (relative to the externally applied magnetic field) and strength of the magnetic field generated by a stripe domain and its surrounding environment, which is approximately 22  $\mu$ T. In particular, at the top of Fig. 3(c), we show ODMR spectra for two specific cases (i.e., imaging pixels): the first one shows the magnetic field originating from the center of a magnetic stripe domain, while the second one shows the magnetic field originating from the surface of the sample (far away from a stripe domain). The observed ODMR frequency splittings (between the sets of five Lorentzians corresponding to the N-V  $m_s = -1$  and  $m_s = +1$  spin states) are reduced for the pixels that image the magnetic fields from the stripe domains compared to the pixels imaging surfaces without stripe domains; in this case [Fig. 3(a)], the surface magnetization of the sample is aligned with the externally applied

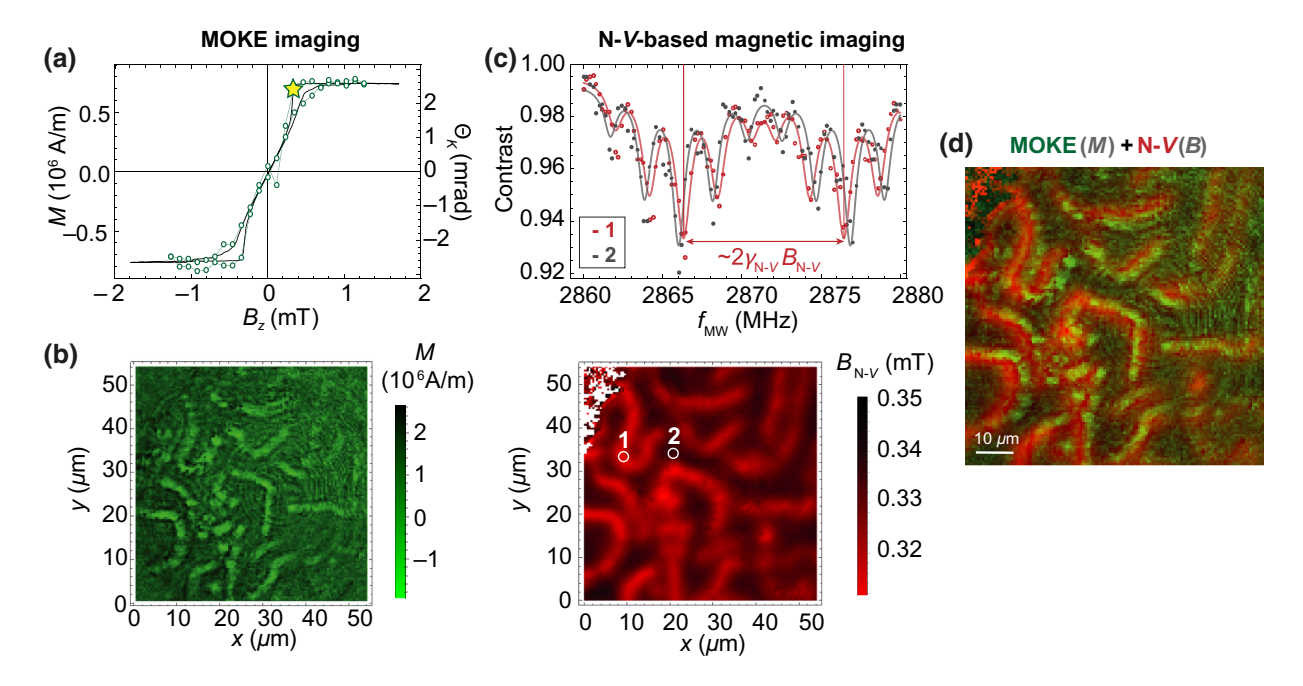


FIG. 3. Magnetization and magnetic field imaging using MOKE and N-V-based magnetic field imaging. (a) The out-of-plane magnetization curve of the magnetic sample (open green circles) and, for comparison, the magnetization curve obtained using a commercial MOKE microscope (black line). The starred point denotes the position on the hysteresis curve where the MOKE and N-V-based magnetic images are obtained. (b) A MOKE image for an applied external magnetic field of  $B_z = 0.329$  mT. (c) ODMR spectra for two different positions within the imaged FOV (the points are measured data while the lines represent the best fit for these data sets) and imaging of the resulting magnetic fields generated from the sample for an external field of  $B_z = 0.329$  mT (the magnetic field is obtained by fitting the ODMR spectra for each pixel). (d) N-V (red) and MOKE (green) images overlapped.

magnetic field, while within the stripe domains the magnetization is reversed (thus resulting in an overall reduced observed magnetic field and, hence, in a reduction in the observed ODMR splittings). We note here that maximum magnetic (stray) field values are attainable at the center of the magnetically imaged stripe domains due to the stand-off distance between the N-V layer and the surface of the sample (approximately 3–4  $\mu$ m), taking into consideration that the magnetic domains have a width of approximately 3  $\mu$ m (for larger domains, the main magnetic contrast would be expected to be closer to the observed walls of a domain).

It should be noted that the effective bandwidth of each measurement in our imaging configuration is different. While a MOKE image takes approximately 0.5 s, an N-V image (for which, here, we record the full ODMR spectrum) takes approximately 300 s. The time required to record an N-V-based magnetic image could be significantly decreased to approximately 3 s by recording magnetic images at a single-frequency and using a calibration (e.g., an image at an off-resonant excitation frequency) to get quantitative information about the magnetic field, but this is beyond the scope of this work.

Finally, in Fig. 3(d) we present the MOKE and N-V magnetic images overlapped to demonstrate the complementary character of the two imaging modalities, while it

also allows us to clearly investigate the differences in the observed sizes of the stripe domains between the two imaging modalities. These differences are related to the offset distance between the diamond and the magnetic sample (approximately 3–4  $\mu$ m), which results in blurring of the observed features in the (N-V) magnetic image. This also verifies that the resolution of the N-V magnetic image is currently determined by the size of this offset distance and not by the optical resolution of the microscope. We also note here that this becomes consequential when the stripe domains are dense, i.e., when the distance between the stripe domains is smaller than the resolution of N-V-magnetic imaging, resulting in noticeable differences between the N-V magnetic and MOKE images. In such cases, the magnetic fields from different domains might, for example, add up and it will not be easily possible to reconstruct the magnetic topology of the domain structure. However, such an issue can be resolved (in future implementations) by minimizing the distance between the diamond surface and the magnetic sample [for instance, one way to minimize this gap is to directly deposit (twodimensional) magnetic materials onto the diamond surface [41]]. Furthermore, we observe in our images slight deviations from perfect overlap between the observed magnetization and magnetic field maps from stripe features that reside at the edges of our FOV. We believe this is the result of a combination of offset-related magnetic field gradients (of the field generated by the domains) and off-axis aberrations. Further investigations are required to resolve this issue.

### V. DISCUSSION AND CONCLUSIONS

We present a platform for wide-field imaging of the magnetization and resulting magnetic fields of magnetic structures using engineered diamond magnetic sensors and an optical setup that allows for both measurement modalities. Our work extends recently developed N-V-magnetic imaging techniques used to study magnetic systems by demonstrating how the addition of polarization analysis can incorporate simultaneous information about the magnetization of the sample.

Possible extensions to the current experimental setup are possible for both the MOKE- and N-V-based imaging parts. The N-V-based imaging, for example, can be extended to the zero-field regime by implementing recently developed measurement schemes [42] or even be operated in a MW-free modality [43,44]. Furthermore, while the setup is currently only sensitive to out-of-plane magnetizations (polar MOKE), it can be extended to measurements of longitudinal and transverse MOKEs, i.e., the measurement of in-plane magnetizations, by illuminating the sample at an angle [25]. To do so, the incorporation of field coils for the generation of in-plane magnetic fields would be necessary. Most importantly, the angled illumination allows for truly concurrent acquisition of N-V and MOKE images, as the reflected beam and the fluorescence are now detected in different areas of the camera (or independently imaged from their respective optical paths).

Magnetic structures, and generally correlated and topological electron systems, present crucial technological opportunities for information storage and computation and their inherent nonvolatility makes them central to energy-related research and associated technologies. Moreover, our understanding of condensed-matter physics is greatly affected by these technologies that exploit the topology of spin structures, as is the case with technologies that exploit the topology of the physical and electronic structure of materials. Our primary goal is to develop an instrument that is ideal for the research and development of these technologies and the study of related emergent phenomena.

# ACKNOWLEDGMENTS

This work was supported by the European Union FET (Future and Emerging Technologies) Open Flagship "Advancing Science and TEchnology thRough dIamond Quantum Sensing" (ASTERIQS) project (Action 820394), the Dynamics and Topology Center funded by the State of Rhineland Palatinate, the German Federal Ministry

of Education and Research (BMBF) within the Quantumtechnologien program (Grants No. FKZ 13N14439 and No. FKZ 13N15064), as well as the German Research Foundation (SFB TRR 173 Spin+X project A01 No. 268565370 and SPP 2137 Skyrmionics No. 403502522) and the ERC under the European Union's Horizon 2020 research and innovation programme ERC-Syn-2018 3D MAGiC (Grant Agreement No. 856538). Y.D. acknowledges support by the Alexander von Humboldt Foundation. K.M.C.F. and Z.K. acknowledge support by the University of Washington Molecular Engineering and Materials Center, with funding from the National Science Foundation (NSF) Materials Research Science and Engineering Centers (MRSEC) program (Grant No. DMR-1719797).

- [1] R. L. Stamps, S. Breitkreutz, J. Åkerman, A. V. Chumak, Y.-C. Otani, G. E. W. Bauer, J.-U. Thiele, M. Bowen, S. A. Majetich, M. Kläui, I. L. Prejbeanu, B. Dieny, N. M. Dempsey, and B. Hillebrands, The 2014 magnetism roadmap, J. Phys. D: Appl. Phys. 47, 333001 (2014).
- [2] D. Sander, S. O. Valenzuela, D. Makarov, C. H. Marrows, E. E. Fullerton, P. Fischer, J. McCord, P. Vavassori, S. Mangin, P. Pirro, B. Hillebrands, A. D. Kent, T. Jungwirth, O. Gutfleisch, C. G. Kim, and A. Berger, The 2017 magnetism roadmap, J. Phys. D: Appl. Phys. 50, 363001 (2017).
- [3] F. El Gabaly, S. Gallego, C. Mutildenoz, L. Szunyogh, P. Weinberger, C. Klein, A. K. Schmid, K. F. McCarty, and J. de la Figuera, Imaging Spin-Reorientation Transitions in Consecutive Atomic Co Layers on Ru(0001), Phys. Rev. Lett. **96**, 147202 (2006).
- [4] N. Rougemaille and A. K. Schmid, Magnetic imaging with spin-polarized low-energy electron microscopy, Eur. Phys. J. Appl. Phys. **50**, 20101 (2010).
- [5] P. Fischer, Magnetic imaging with polarized soft x-rays,J. Phys. D: Appl. Phys. 50, 313002 (2017).
- [6] S. Bonetti, X-ray imaging of spin currents and magnetisation dynamics at the nanoscale, J. Phys.: Condens. Matter 29, 133004 (2017).
- [7] J. A. Slides, J. L. Garbini, K. J. Bruland, D. Rugar, O. Züger, S. Hoen, and C. S. Yannoni, Magnetic resonance force microscopy, Rev. Mod. Phys. 67, 249 (1995).
- [8] I. Lee, Y. Obukhov, G. Xiang, A. Hauser, F. Yang, P. Banerjee, D. V. Pelekhov, and P. C. Hammel, Nanoscale scanning probe ferromagnetic resonance imaging using localized modes, Nature 466, 845 (2010).
- [9] J. R. Kirtley and J. P. Wikswo Jr., Scanning squid microscopy, Annu. Rev. Mater. Sci. 29, 117 (1999).
- [10] D. Vasyukov, Y. Anahory, L. Embon, D. Halbertal, J. Cuppens, L. Neeman, A. Finkler, Y. Segev, Y. Myasoedov, M. L. Rappaport, M. E. Huber, and E. Zeldov, A scanning superconducting quantum interference device with single electron spin sensitivity, Nat. Nanotechnol. 8, 639 (2013).
- [11] F. Casola, T. van der Sar, and A. Yacoby, Probing condensed matter physics with magnetometry based on nitrogen-vacancy centres in diamond, Nat. Rev. Mater. 3, 17088 (2018).

- [12] J.-P. Tetienne, T. Hingant, L. J. Martínez, S. Rohart, A. Thiaville, L. H. Diez, K. Garcia, J.-P. Adam, J.-V. Kim, J.-F. Roch, I. M. Miron, G. Gaudin, L. Vila, B. Ocker, D. Ravelosona, and V. Jacques, The nature of domain walls in ultrathin ferromagnets revealed by scanning nanomagnetometry, Nat. Commun. 6, 6733 (2015).
- [13] J.-P. Tetienne, T. Hingant, J.-V. Kim, L. H. Diez, J.-P. Adam, K. Garcia, J.-F. Roch, S. Rohart, A. Thiaville, D. Ravelosona, and V. Jacques, Nanoscale imaging and control of domain-wall hopping with a nitrogen-vacancy center microscope, Science 344, 1366 (2014).
- [14] I. Gross, W. Akhtar, V. Garcia, L. J. Martínez, S. Chouaieb, K. Garcia, C. Carrétéro, A. Barthélémy, P. Appel, P. Maletinsky, J.-V. Kim, J. Y. Chauleau, N. Jaouen, M. Viret, M. Bibes, S. Fusil, and V. Jacques, Real-space imaging of non-collinear antiferromagnetic order with a single-spin magnetometer, Nature 549, 252 (2017).
- [15] I. Gross, L. J. Martínez, J.-P. Tetienne, T. Hingant, J.-F. Roch, K. Garcia, R. Soucaille, J. P. Adam, J.-V. Kim, S. Rohart, A. Thiaville, J. Torrejon, M. Hayashi, and V. Jacques, Direct measurement of interfacial Dzyaloshinskii-Moriya interaction in x|CoFeB|MgO heterostructures with a scanning NV magnetometer (x = Ta, TaN, and W), Rev. B **94**, 064413 (2016).
- [16] I. Gross, W. Akhtar, A. Hrabec, J. Sampaio, L. J. Martínez, S. Chouaieb, B. J. Shields, P. Maletinsky, A. Thiaville, S. Rohart, and V. Jacques, Skyrmion morphology in ultrathin magnetic films, Phys. Rev. Mater. 2, 024406 (2018).
- [17] A. Jenkins, M. Pelliccione, G. Yu, X. Ma, X. Li, K. L. Wang, and A. C. Bleszynski Jayich, Single-spin sensing of domain-wall structure and dynamics in a thin-film skyrmion host, Phys. Rev. Mater. 3, 083801 (2019).
- [18] L. M. Pham, D. Le Sage, P. L. Stanwix, T. K. Yeung, D. Glenn, A. Trifonov, P. Cappellaro, P. R. Hemmer, M. D. Lukin, H. Park, A. Yacoby, and R. L. Walsworth, Magnetic field imaging with nitrogen-vacancy ensembles, New J. Phys. 13, 045021 (2011).
- [19] M. Chipaux, A. Tallaire, J. Achard, S. Pezzagna, J. Meijer, V. Jacques, J.-F. Roch, and Th. Debuisschert, Magnetic imaging with an ensemble of nitrogen-vacancy centers in diamond, Eur. Phys. J. D 69, 166 (2015).
- [20] D. R. Glenn, K. Lee, H. Park, R. Weissleder, A. Yacoby, M. D. Lukin, H. Lee, R. L. Walsworth, and C. B. Connolly, Single-cell magnetic imaging using a quantum diamond microscope, Nat. Methods 12, 736 (2015).
- [21] I. Fescenko, A. Laraoui, J. Smits, N. Mosavian, P. Kehayias, J. Seto, L. Bougas, A. Jarmola, and V. M. Acosta, Diamond Magnetic Microscopy of Malarial Hemozoin Nanocrystals, Phys. Rev. Appl. 11, 034029 (2019).
- [22] J. M. Schloss, J. F. Barry, M. J. Turner, and R. L. Walsworth, Simultaneous Broadband Vector Magnetometry Using Solid-State Spins, Phys. Rev. Appl. 10, 034044 (2018).
- [23] Y. Dovzhenko, F. Casola, S. Schlotter, T. X. Zhou, F. Büttner, R. L. Walsworth, G. S. D. Beach, and A. Yacoby, Magnetostatic twists in room-temperature skyrmions explored

- by nitrogen-vacancy center spin texture reconstruction, Nat. Commun. 9, 2712 (2018).
- [24] A. Y. Meltzer, E. Levin, and E. Zeldov, Direct Reconstruction of Two-Dimensional Currents in Thin Films from Magnetic-Field Measurements, Phys. Rev. Appl. 8, 064030 (2017).
- [25] J. McCord, Progress in magnetic domain observation by advanced magneto-optical microscopy, J. Phys. D: Appl. Phys. 48, 333001 (2015).
- [26] G. Chatzidrosos, A. Wickenbrock, L. Bougas, N. Leefer, T. Wu, K. Jensen, Y. Dumeige, and D. Budker, Miniature Cavity-Enhanced Diamond Magnetometer, Phys. Rev. Appl. 8, 044019 (2017).
- [27] E. Bourgeois, A. Jarmola, P. Siyushev, M. Gulka, J. Hruby, F. Jelezko, D. Budker, and M. Nesladek, Photoelectric detection of electron spin resonance of nitrogen-vacancy centres in diamond, Nat. Commun. 6, 8577 (2015).
- [28] S. Felton, A. M. Edmonds, M. E. Newton, P. M. Martineau, D. Fisher, D. J. Twitchen, and J. M. Baker, Hyperfine interaction in the ground state of the negatively charged nitrogen vacancy center in diamond, Phys. Rev. B 79, 075203 (2009).
- [29] S. Steinert, F. Dolde, P. Neumann, A. Aird, B. Naydenov, G. Balasubramanian, F. Jelezko, and J. Wrachtrup, High sensitivity magnetic imaging using an array of spins in diamond, Rev. Sci. Instrum. 81, 043705 (2010).
- [30] D. A. Simpson, J.-P. Tetienne, J. M. McCoey, K. Ganesan, L. T. Hall, S. Petrou, R. E. Scholten, and L. C. L. Hollenberg, Magneto-optical imaging of thin magnetic films using spins in diamond, Sci. Rep. 6, 22797 (2016).
- [31] D. Le Sage, K. Arai, D. R. Glenn, S. J. DeVience, L. M. Pham, L. Rhan-Lee, M. D. Lukin, A. Yacobi, A. Komeili, and R. L. Walsworth, Optical imaging of living cells, Nature 496, 486 (2013).
- [32] Y. Schlussel, T. Lenz, D. Rohner, Y. Bar-Haim, L. Bougas, D. Groswasser, M. Kieschnick, E. Rozenberg, L. Thiel, A. Waxman, J. Meijer, P. Maletinsky, D. Budker, and R. Folman, Wide-Field Imaging of Superconductor Vortices with Electron Spins in Diamond, Phys. Rev. Appl. 10, 034032 (2018).
- [33] A. Nowodzinski, M. Chipaux, L. Toraille, V. Jacques, J.-F. Roch, and T. Debuisschert, Nitrogen-vacancy centers in diamond for current imaging at the redistributive layer level of integrated circuits, Microelectron. Reliab. 55, 1549 (2015).
- [34] S. E. Lillie, N. Dontschuk, D. A. Broadway, D. L. Creedon, L. C. L. Hollenberg, and J.-P. Tetienne, Imaging Graphene Field-Effect Transistors on Diamond Using Nitrogen-Vacancy Microscopy, Phys. Rev. Appl. 12, 024018 (2019).
- [35] J. Zázvorka, F. Jakobs, D. Heinze, N. Keil, S. Kromin, S. Jaiswal, K. Litzius, G. Jakob, P. Virnau, D. Pinna, K. Everschor-Sitte, L. Rózsa, A. Donges, U. Nowak, and M. Kläui, Thermal skyrmion diffusion used in a reshuffler device, Nat. Nanotechnol. 14, 658 (2019).
- [36] G. Yu, P. Upadhyaya, X. Li, W. Lu, S. K. Kim, K. L. Wong, Y. Tserkovnyak, P. K. Amiri, and K. L. Wang, Roomtemperature creation and spin-orbit torque manipulation of skyrmions in thin films with engineered asymmetry, Nano Lett. 16, 1981 (2016).

- [37] B.-F. Miao, Y.-T. Millev, L. Sun, B. You, W. Zhang, and H.-F. Ding, Thickness-driven spin reorientation transition in ultrathin films, Sci. China Phys. Mech. Astron. **56**, 70 (2013).
- [38] I. Lemesh, K. Litzius, M. Böttcher, P. Bassirian, N. Kerber, D. Heinze, J. Zázvorka, F. Büttner, L. Caretta, M. Mann, M. Weigand, S. Finizio, J. Raabe, M.-Y. Im, H. Stoll, G. Schütz, B. Dupé, M. Kläui, and G. S. D. Beach, Current-induced skyrmion generation through morphological thermal transitions in chiral ferromagnetic heterostructures, Adv. Mater. 30, 1805461 (2018).
- [39] E. E. Kleinsasser, M. M. Stanfield, J. K. Q. Banks, Z. Zhu, W.-D. Li, V. M. Acosta, H. Watanabe, K. M. Itoh, and K.-M. C. Fu, High density nitrogen-vacancy sensing surface created via He<sup>+</sup> ion implantation of <sup>12</sup>C diamond, Appl. Phys. Lett. 108, 202401 (2016).
- [40] J. F. Barry, M. J. Turner, J. M. Schloss, D. R. Glenn, Y. Song, M. D. Lukin, H. Park, and R. L. Walsworth, Optical magnetic detection of single-neuron action potentials using quantum defects in diamond, Proc. Natl. Acad. Sci. 113, 14133 (2016).

- [41] I. Lovchinsky, J. D. Sanchez-Yamagishi, E. K. Urbach, S. Choi, S. Fang, T. I. Andersen, K. Watanabe, T. Taniguchi, A. Bylinskii, E. Kaxiras, P. Kim, H. Park, and M. D. Lukin, Magnetic resonance spectroscopy of an atomically thin material using a single-spin qubit, Science 355, 503 (2017).
- [42] H. Zheng, J. Xu, G. Z. Iwata, T. Lenz, J. Michl, B. Yavkin, K. Nakamura, H. Sumiya, T. Ohshima, J. Wrachtrup, A. Wickenbrock, and D. Budker, Zero-Field Magnetometry Based on Nitrogen-Vacancy Ensembles in Diamond, Phys. Rev. Appl. 11, 064068 (2019).
- [43] H. Zheng, Z. Sun, G. Chatzidrosos, C. Zhang, K. Nakamura, H. Sumiya, T. Ohshima, J. Isoya, J. Wrachtrup, A. Wickenbrock, and D. Budker, Microwave-free vector magnetometry with nitrogen-vacancy centers along a single axis in diamond, Phys. Rev. Appl 13, 044023 (2020).
- [44] A. Wickenbrock, H. Zheng, L. Bougas, N. Leefer, S. Afach, A. Jarmola, V. M. Acosta, and D. Budker, Microwave-free magnetometry with nitrogen-vacancy centers in diamond, Appl. Phys. Lett. 109, 053505 (2016).